

# Reynolds-Stress Modelling of Subsonic and Transonic Inlet Stall Compared to Measurements

Axel Probst,\*

*DLR Göttingen, C<sup>2</sup>A<sup>2</sup>S<sup>2</sup>E, 37073 Göttingen, Germany*

Sonja Schulze, † Christian J. Kähler, ‡

*UniBW München, Institute of Fluid Mechanics and Aerodynamics, 85577 Neubiberg, Germany*  
and Rolf Radespiel §

*TU Braunschweig, Institute of Fluid Mechanics, 38106 Braunschweig, Germany*

## Abstract

Advanced near-wall Reynolds-stress modelling is applied to the stall of a subsonic flow-through nacelle and a transonic powered engine. For both flows the simulations provide improved predictions of separation onset compared to conventional turbulence models. In the subsonic stall case, mean-flow predictions at very high angles of attack suffer from too low Reynolds-stress levels in the separated region, which can be partly cured by an RSM-based hybrid RANS/LES approach. In the transonic stall cases, industrial coefficients for the inlet distortion are computed in satisfying agreement with measurements.

## Nomenclature

$c_p$	Static pressure coefficient
$d$	Nacelle diameter, m
$H_{12}$	Boundary-layer shape factor
$k$	Turbulent kinetic energy, $\text{m}^2/\text{s}^2$
$l$	Nacelle length, m
$U, V, W$	Mean velocity components, m/s
$\overline{u_i u_j}$	Reynolds-stress tensor, $\text{m}^2/\text{s}^2$
$\alpha$	Angle of attack, °
$\varepsilon, \varepsilon^h$	Total and homogeneous dissipation rate, $\text{m}^2/\text{s}^3$
$\Theta$	Circumferential nacelle angle, °

---

\*Research scientist, E-Mail: axel.probst@dlr.de

†Research scientist.

‡Professor.

§Professor.

# 1 Introduction

Flow separations in engine inlets cause disturbances in the onflow to the subsequent compressor stages and may therefore affect the stability of the core engine. Numerical simulations of a powered engine in crosswind showed the difficulty to predict such distortions using conventional RANS turbulence models [1]. In order to improve predictions of stall phenomena in the design phase, advanced turbulence closures such as Reynolds-stress models (RSM) gain relevance [2], but they still require validation with the aid of suited experimental data.

Within the joint DFG-FOR1066 project, a specific validation experiment on a stalling flow-through nacelle in a low-speed wind tunnel was conducted which provides high-quality measurements of flow-field details using non-intrusive particle image velocimetry (PIV) methods [3]. However, the flow-through setup neglects the transonic flow effects which are encountered in real flight conditions of powered engines. Therefore, the validation strategy for the RSM-based modelling developed in DFG-FOR1066 is extended here from purely subsonic inlet flow [4] to the transonic stall of a powered engine. Suited but less extensive validation data is obtained from off-design studies on the LARA nacelle [5], including industrial design criteria such as peak Mach-numbers at the inlet lip and distortion coefficients of the fan onflow.

Both the sub- and the transonic inlet stall cases are computed with the DLR-TAU code [6], using a recent variant of the near-wall JHh-RSM [7], [2] as well as advanced transition modelling [8]. Moreover, a first application of this approach in the framework of a hybrid RANS/LES simulation [9], [10] to the flow-through nacelle is described, which takes advantage of scale-resolving methods for the strongly separated inlet flow at higher angles of attack.

## 2 Numerical Method

The simulations conducted in this work use the unstructured finite-volume flow solver DLR-TAU [6] for the compressible mean-flow and turbulence equations. It provides second-order accuracy in space, applying a central scheme with matrix dissipation and preconditioning for the low-speed flow-through nacelle and an AUSMDV upwind scheme for the transonic LARA flow case. Implicit dual-time stepping with second-order accuracy is performed for the unsteady simulations (URANS/DES). The physical modelling is briefly outlined as follows.

### 2.1 Low-Reynolds JHh-v2 Reynolds-Stress Model

The JHh-v2 RSM [2] is derived from the Jakirlić-Hanjalić-homogeneous RSM [7] which applies a length-scale-supplying equation for the homogeneous dissipation rate  $\varepsilon^h$  and low-Reynolds damping in order to accurately model near-wall turbulence. In the JHh-v2, the Reynolds-stress equations:

$$\frac{D\overline{u_i u_j}}{Dt} = - \left( \overline{u_i u_k} \frac{\partial U_j}{\partial x_k} + \overline{u_j u_k} \frac{\partial U_i}{\partial x_k} \right) + \Phi_{ij} - \varepsilon_{ij}^h + \frac{1}{2} D_{ij}^\nu + D_{ij}^t \quad , \quad (1)$$

apply a non-linear (i.e. quadratic) model for redistribution  $\Phi_{ij}$  and a generalized-gradient model for turbulent diffusion  $D_{ij}^t$ . An algebraic anisotropy model computes the homogeneous dissipation-rate tensor  $\varepsilon_{ij}^h$  from the scalar value  $\varepsilon^h$ . The latter is provided by an additional transport equation, reading:

$$\frac{D\varepsilon^h}{Dt} = -C_{\varepsilon_1} \frac{\varepsilon^h}{k} \overline{u_i u_j} \frac{\partial U_i}{\partial x_j} - C_{\varepsilon_2} f_\varepsilon \frac{\varepsilon^h \tilde{\varepsilon}^h}{k} + C_{\varepsilon_3} \nu \frac{k}{\varepsilon^h} \overline{u_j u_k} \frac{\partial^2 U_i}{\partial x_j \partial x_l} \frac{\partial^2 U_i}{\partial x_k \partial x_l} + D_\varepsilon + S_l + S_{\varepsilon_4} \quad . \quad (2)$$

Besides a near-wall damping function  $f_\varepsilon$ , constant coefficients  $C_{\varepsilon_1} = 1.44$ ,  $C_{\varepsilon_2} = 1.85$ ,  $C_{\varepsilon_3} = 0.7$  are employed which partly deviate from the original calibration in [7]. The length-scale limiter  $S_l$  and the pressure-gradient term  $S_{\varepsilon_4}$  are additional source terms which sensitize the model to non-equilibrium conditions. A more detailed model description is found in [2].

For a consistent transition behaviour in low-turbulence environments the JHh-v2 RSM is furthermore coupled with a linear-stability-based modelling approach described in [8]. In addition to an  $e^N$  transition-prediction method, the contributions of the 2D Tollmien-Schlichting waves to the statistical Reynolds stresses are computed and inserted in the RANS solution at turbulence onset. As shown in [4], this approach ensures an insensitive transition and separation behaviour of the low-speed inlet flow addressed in Sec. 3, whereas the classic point transition would retain unphysical laminar flow.

## 2.2 RSM-based Hybrid RANS/LES model

To apply the JHh-v2 RSM in a general detached eddy simulation (DES), the (homogeneous) dissipation-rate tensor is multiplied by the ratio of the RANS length scale to the hybrid length scale of the respective DES-model, i.e.

$$\varepsilon_{ij,\text{DDES}}^h = \varepsilon_{ij}^h \cdot \frac{l_{\text{RANS}}}{l_{\text{hyb}}} \quad . \quad (3)$$

In the present study on the low-speed nacelle flow, the hybrid length scale is provided by the algebraic delayed DES approach (ADDES) [9]. It uses the basic delayed-DES definition for  $l_{\text{hyb}}$ :

$$l_{\text{hyb}} = l_{\text{RANS}} - f_d \cdot \max(0, l_{\text{RANS}} - C_{\text{DES}}\Delta) \quad , \quad (4)$$

but replaces the delay function  $f_d$  by a combination of algebraic boundary-layer criteria, which are evaluated along wall-normal lines. In particular, the boundary-layer thickness is computed via the  $\delta_{99}$  criterion in order to fully shield attached boundary layers from so-called modelled-stress depletion ( $f_d = 0$ ). On the other hand, the interface to the LES region is placed near the separation point or line, which is detected based on the boundary-layer shape factor  $H_{12}$  via the criterion  $H_{12} > H_{12,\text{crit}}$ . The critical shape factor to determine separation requires calibration for the respective RANS model and takes a value of  $H_{12,\text{crit}} = 3.2$  for the JHh-v2 RSM.

In the LES region ( $f_d = 1$ ), Eq. (4) reduces to  $l_{\text{hyb}} = C_{\text{DES}}\Delta$ , where  $\Delta$  is the maximum local grid spacing and  $C_{\text{DES}}$  is a model constant, calibrated as  $C_{\text{DES}} = 1.1$  for the JHh-v2 RSM. Moreover, its low-Reynolds modelling is explicitly deactivated in the LES region in order to avoid excessive damping of the sub-grid stresses. More details are found in [10].

## 3 Subsonic Flow-Through Nacelle

In order to acquire high-quality validation data on inlet separation, a specific wind-tunnel experiment on a subsonic flow-through nacelle at stall conditions was performed within DFG-FOR1066. As the flow-through setup is restricted to much lower mass-flow rates and velocities compared to realistic flight conditions, the aerodynamic design of the axisymmetric nacelle geometry was aimed to mimic the stall behaviour of a powered engine [11].

The experiments were performed in the Atmospheric Windtunnel Munich (AWM) at an onflow Mach number of 0.11 and a Reynolds number of  $1.34 \cdot 10^6$  based on the nacelle length. To avoid premature laminar flow separation in the inlet, a carefully-designed method to trip transition

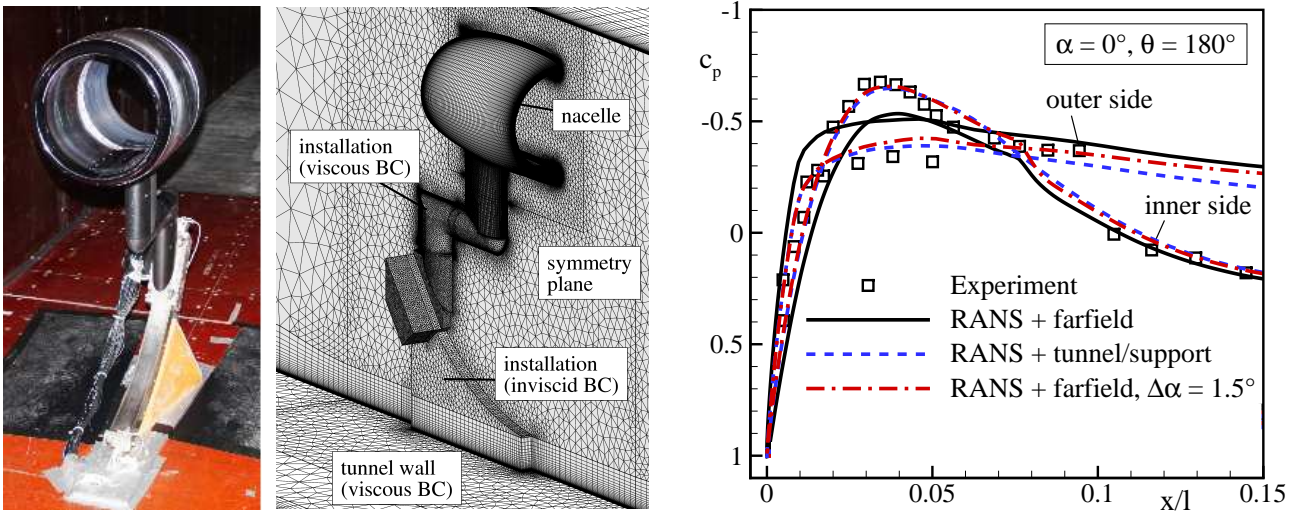


Figure 1: Photo of the experiment on the flow-through nacelle and corresponding numerical mesh (left); sensitivities of the surface pressure in the lower cut section around  $\alpha = 0^\circ$  (right).

at the leading edge was applied. Permanent orifices spread across the nacelle's circumference are fed with a suitable mass flow and thus ensure reproducible measurement conditions. The sensitivity of the inlet flow to changes in the experimental setup was analyzed thoroughly to provide a high-quality and up to now unique validation data basis. The wind tunnel experiments yield information about the topology of the separated inlet flow and comprise oil flow pictures, static pressure measurements as well as different kinds of PIV measurements [3]. The dynamics of the separated inlet flow are captured by employing unsteady pressure transducers and time-resolved PIV measurements.

Due to blocking effects caused by the wind-tunnel model installations shown in Fig. 1 (left), an angle-of-attack correction of the measurement data is required when comparing to simulations in free-flight conditions. This was first observed in RANS studies of the isolated nacelle with farfield boundaries at  $\alpha = 0^\circ$ , which yield a significant and systematic offset to the measured pressure distribution, see Fig. 1 (right). Besides including the wind-tunnel walls and the model support in the simulation as shown in Fig. 1 (left), the error could also be reduced by increasing the angle-of-attack by  $\Delta\alpha = 1.5^\circ$  in a much less expensive farfield simulation, see Fig.1 (right). This  $\alpha$ -correction was later broadly confirmed by PIV measurements and is therefore applied to the experimental data in the validation of the simulations with farfield conditions.

### 3.1 RANS Simulations of the Stall Process

The (U)RANS simulations of the nacelle flow were performed on a hybrid mesh with 4.95 million grid points for the symmetric half model in farfield conditions, which was shown to yield low discretization errors in a preceding refinement study [4]. Throughout the attached flow regime up to at least  $\alpha = 19^\circ$ , a variety of different turbulence models were found to agree equally well with measurements. Therefore, the present validation is focused on the onset of separation and the subsequent development for further increased angle of attack. Apart from the JHh-v2 RSM with transition prediction and modelling as described in Sec. 2, the original RSM variant JHh-v1, which was initially used as standard model within DFG-FOR1066, and the well-known Menter  $k-\omega$  SST are used as reference. All other aspects of the numerical setup

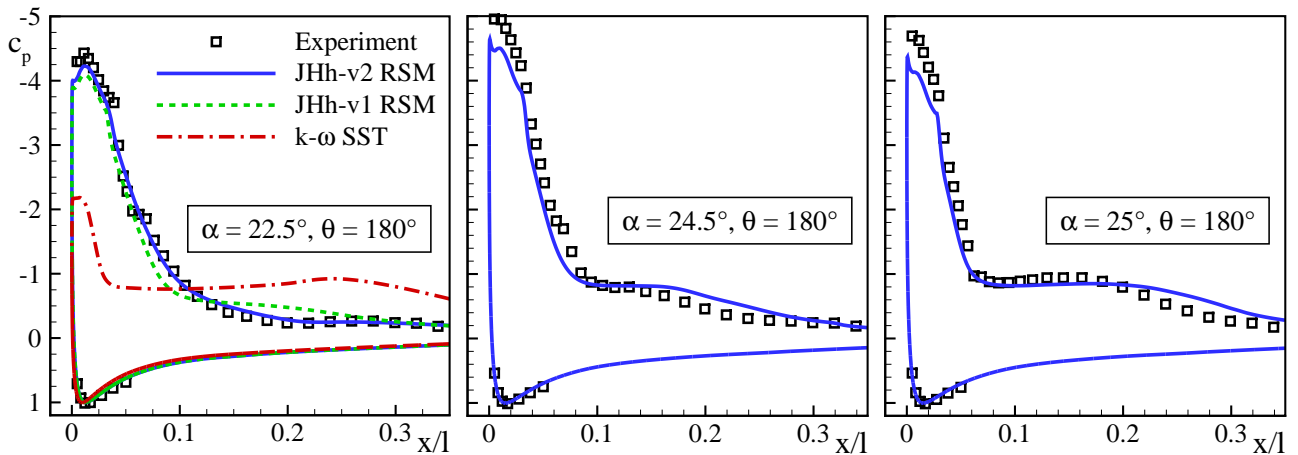


Figure 2: Pressure distributions in the lower cut section of the flow-through nacelle.

correspond to earlier investigations of this flow [4].

Figure 2 depicts surface-pressure distributions in the lower inlet cut section  $\Theta = 180^\circ$  around separation onset, which is indicated by the formation of a pressure plateau and a reduced suction pressure at the nose. In contrast to the SST model, which shows a drastic break-down of the suction peak already at  $\alpha = 22.5^\circ$ , both JHh-RSM variants mostly retain the pressure distribution up to this point. However, also the JHh-v1 RSM separates somewhat too early as indicated by an incipient pressure plateau at  $\alpha = 22.5^\circ$ , whereas the experiment features no such behaviour until  $\alpha = 24.5^\circ$ .

Only the recalibrated RSM variant JHh-v2 roughly follows the experimental trend and delays separation onset until  $\alpha = 24^\circ$ . This is achieved by a reduced net-production of turbulent dissipation in adverse pressure gradients compared to the JHh-v1 RSM, which results in somewhat higher levels of stabilizing Reynolds stresses in boundary layers approaching separation [2].

However, from  $\alpha = 24.5^\circ$  onwards a slight but increasing overestimation of both the pressure plateau and the suction-peak reduction is observed in Fig. 2. This is further studied by comparing computed mean streamlines with experimental oil-flow visualizations in Fig. 3. Unlike the JHh-v1 RSM in [4], the JHh-v2 RSM is not only able to qualitatively reproduce the measured “owl-eye“ separation pattern in the inlet, but also roughly matches its size at the same (corrected) angle of attack. However, the computed separation pattern grows a bit quicker than measured and forms a secondary vortex pattern with an out-of-plane saddle point at  $\alpha = 25^\circ$ , which is not indicated by the experiment (including higher angles of attack not shown here).

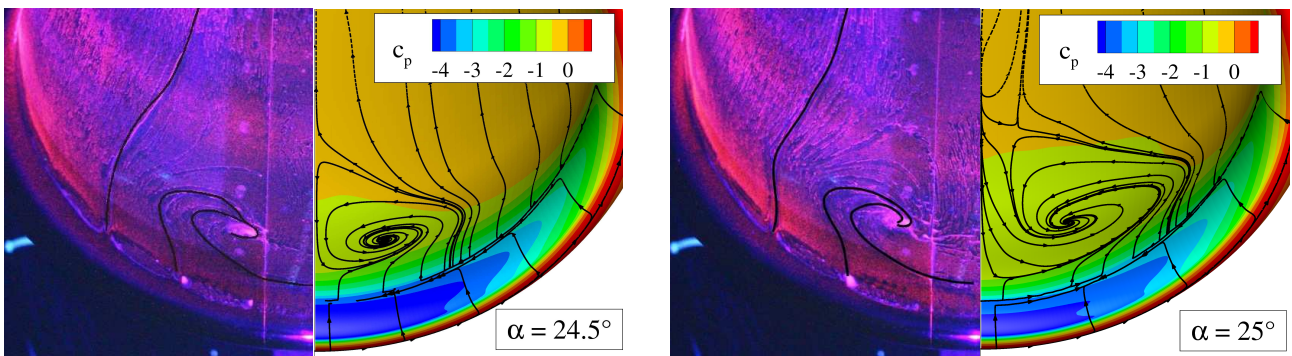


Figure 3: Oil-flow pictures and results of the JHh-v2 RSM (mean pressure and streamlines).

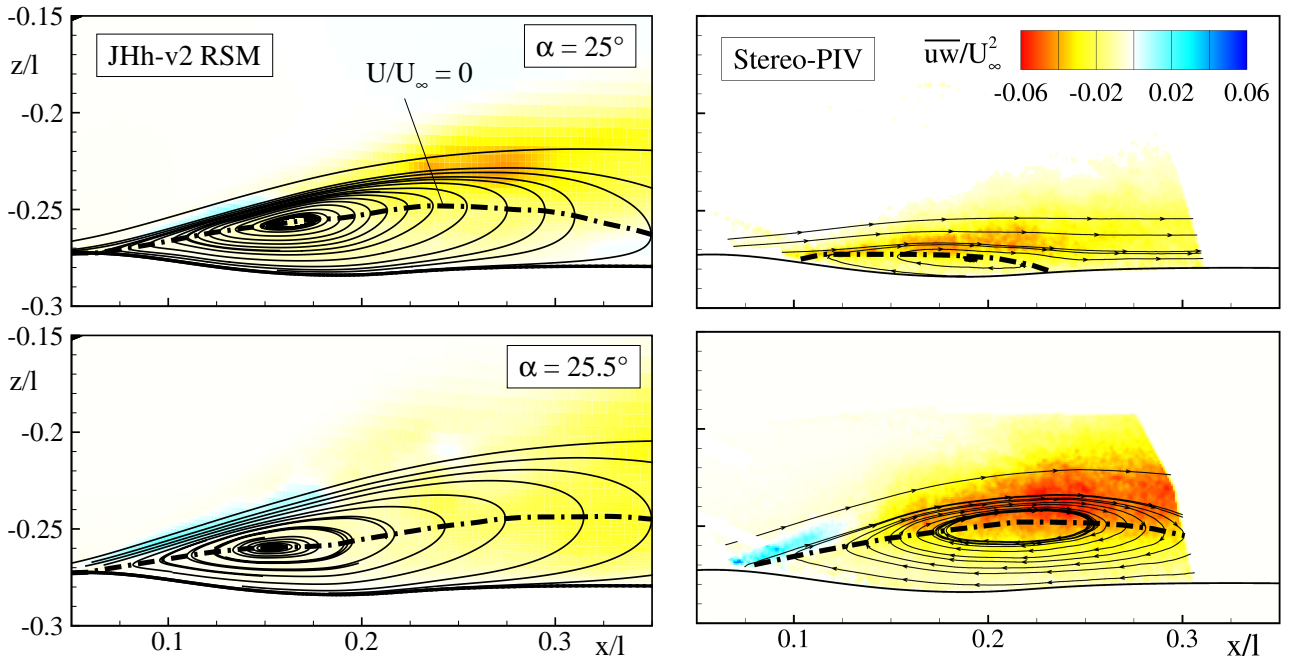


Figure 4: Mean streamlines and Reynolds shear stress in the symmetry plane from computations (left) and measurements (right). The isoline  $U/U_\infty = 0$  marks the recirculation region.

Recent stereoscopic PIV (SPIV) measurements in the symmetry plane of the lower inlet region allow a more detailed analysis and assessment of the modelling approach. Note that separation onset was found to be sensitive to the experimental setup and is shifted to somewhat higher angles of attack in the SPIV measurements. Thus, for a "fair" assessment of the simulation, the results in Fig. 4 should be compared at a similar separation size, which is indicated by the isoline  $U/U_\infty = 0$ . Nonetheless, comparing  $\alpha = 25^\circ$  from the simulation with  $\alpha = 25.5^\circ$  from the experiment, the JHh-v2-RSM URANS underestimates the maximum magnitude of (negative) turbulent shear-stress by roughly 30 %. While the experiment locates this maximum close to the circulation centre and forms a nearly symmetric separation bubble, the simulation shifts the vortex core upstream and delays closure of the bubble. Moreover, the JHh-v2 RSM at  $\alpha = 25.5^\circ$  yields a further reduced magnitude of the Reynolds shear stress, which also appears to be smeared over a wider region. This may be attributed to the large-scale unsteadiness of the later separation encountered in the URANS computations.

Briefly summarized, the updated JHh-RSM-based simulation approach is able to capture separation onset in the subsonic inlet flow close to experimental uncertainty. At higher angles of attack, though, a too low level of turbulent shear stress in the separated area causes deviations from the measured flow topology.

### 3.2 Hybrid RANS/LES Simulation at Stall

As described in the previous section, the remaining deficiencies of the RSM-based URANS approach are mainly associated with the underpredicted level of Reynolds-shear stress in the separated flow region. This corresponds to findings on other flows involving massive separation, such as URANS simulations of a backward-facing step in [10] which show delayed reattachment for the JHh-v2 RSM. However, applying the JHh-v2 RSM within a hybrid RANS/LES approach clearly improved the Reynolds-stress onset and the separation size behind the step [10]. The same approach is adopted here to assess its potential for subsonic inlet stall.

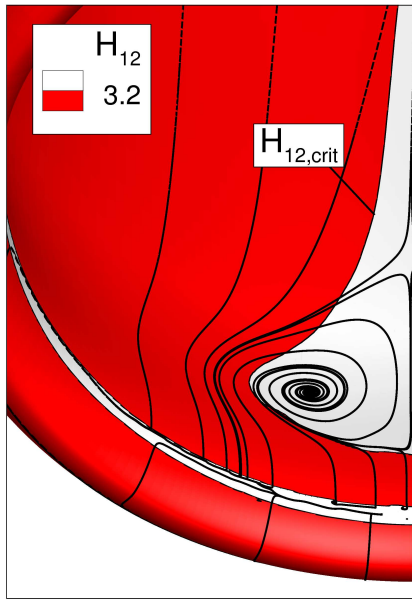


Figure 5: Shape-factor-based separation criterion in the nacelle for a JHh-v2-RSM RANS solution at  $\alpha = 24.5^\circ$ .

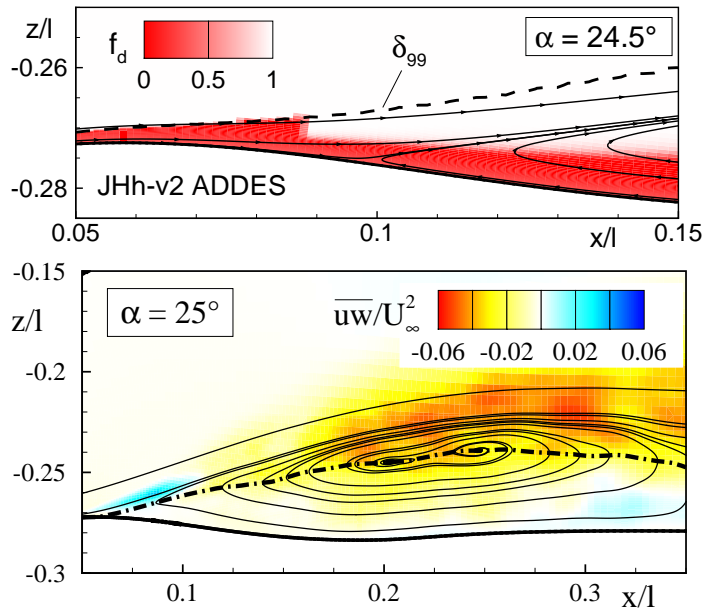


Figure 6: RANS/LES-sensor function at separation point based on the RANS solution from Fig. 5 (top); mean streamlines and Reynolds shear stress computed with JHh-v2 ADDES at  $\alpha = 25^\circ$  (bottom).

In order to account for the characteristics of the pressure-induced separation from the smooth inlet surface, the RANS/LES regions are defined using the algebraic delayed DES (ADDES) described in Sec. 2.2. As shown in Fig. 5 for a steady RANS solution at  $\alpha = 24.5^\circ$ , the separation criterion based on  $H_{12} > H_{12,crit} = 3.2$ , which was originally designed and calibrated for plane 2D flows, works remarkably well in detecting the footprint of the 3D recirculation in the inlet. The laminar separation bubble near the leading edge is captured as well, but resolving laminar-turbulent transition via LES is not subject of the present study. Therefore, in the actual ADDES computation this region is manually fixed in RANS mode and modelled the same way as in the URANS simulations (see Sec. 3.1). According to Fig. 6 (top) the ADDES sensor function  $f_d$  from Eq. (4) safely keeps the attached boundary layer in RANS mode ( $f_d = 0$ ), while an abrupt switching to LES/DES mode ( $f_d = 1$ ) occurs close to separation onset. Note, that the pronounced near-wall RANS-mode region downstream of the separation point is only present in this intermediate computational result just after initializing the transition from URANS to LES and will reduce during the unsteady ADDES computation.

Apart from being doubled w.r.t to the symmetry plane, the same mesh as in the (U)RANS studies is applied. Though probably not providing sufficient resolution in all resolved flow areas, the crucial lower inlet region can be considered to meet the basic requirements of a DES (i.e. mostly isotropic cell spacing). Accordingly, the time step of  $\Delta t \cdot U_\infty / l = 6.25 \cdot 10^{-4}$  is adjusted to locally ensure a convective CFL number below 1 in the separated area.

A single hybrid simulation is performed at  $\alpha = 25^\circ$  which not only combines advanced Reynolds-stress modelling with a novel algebraic DDES, but also includes the linear-stability-based transition prediction and modelling approach as described in Sec. 2.1. Due to the high computational costs the simulation time is confined to 8 convective time units  $T_{conv} = l/U_\infty$ , providing a limited but sufficient statistical certainty for a first validation.

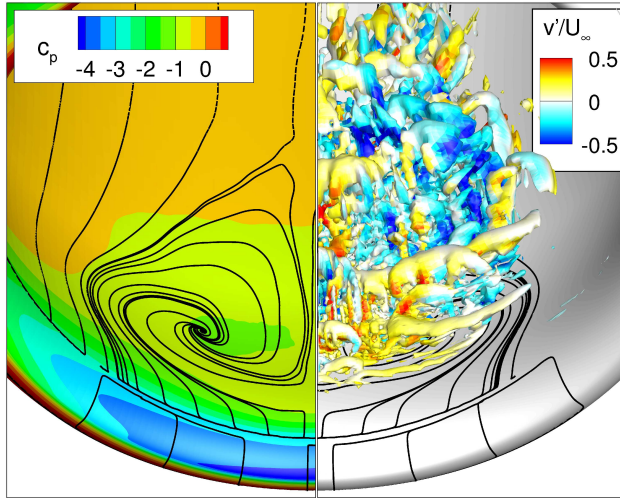


Figure 7: Mean pressure and streamlines (left) and turbulent structures coloured by spanwise velocity fluctuations (right), JHh-v2 ADDES at  $\alpha = 25^\circ$ .

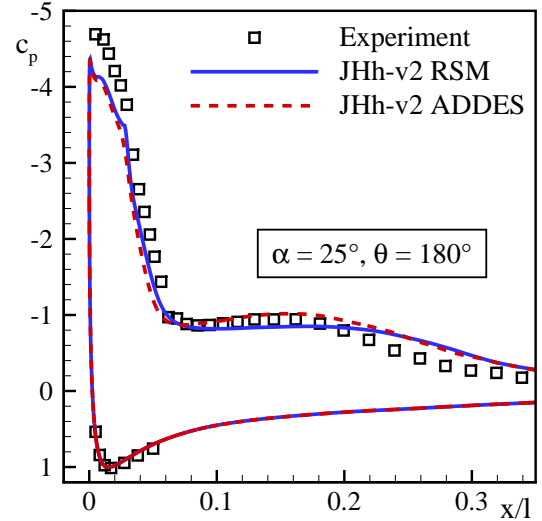


Figure 8: Mean surface pressure distribution in the symmetry plane at  $\alpha = 25^\circ$ .

## Results of JHh-v2 ADDES

Evaluating the time-averaged flow at the end of the JHh-v2-ADDES computation, several significant differences are observed in comparison to the URANS results. Although the separation size at  $\alpha = 25^\circ$  is approximately retained, the Reynolds shear stress in the symmetry plane in Fig. 6 (bottom) reaches significantly higher levels than the corresponding JHh-v2-RSM URANS simulation shown in Fig. 4. As a consequence, the recirculation centre is shifted downstream and is divided into a pair of neighbouring vortices. It may be expected, though, that these two vortices would merge after a longer statistical averaging time. In a "fair" comparison to the experiment at a similar separation size, i.e.  $\alpha = 25.5^\circ$  for PIV in Fig. 4, the JHh-v2-ADDES result agrees quite well with the measured mean-flow topology and Reynolds-stress distribution. The still slightly underestimated resolved shear stress might be further increased using a finer grid resolution in the LES region. A qualitative assessment of the instantaneous Q-criterion in Fig. 7 (right) shows a substantial amount of turbulent structures in the separation region. Neither here, nor in the Reynolds stress in Fig. 6 (bottom), a so-called "grey area" of delayed transition from modelled to resolved turbulence is noticed, which is often observed in incipient pressure-induced separation [10].

According to the mean surface streamlines in Fig. 7 (left) the full 3D-nacelle computation also converges to the owl-eye separation pattern observed in the experiment (see Fig. 3). However, due to the limited averaging time, a fully symmetric mean solution has not yet been reached. Unlike the URANS simulation at  $\alpha = 25^\circ$  with its questionable secondary vortex formation (see Fig. 3), only a single saddle point is formed near the symmetry plane, which sensibly confines the primary vortex pair on the surface. Note that this saddle point is slightly shifted outwards in Fig. 7 (left) due to the mentioned asymmetry. Finally comparing the mean surface pressure at  $\Theta = 180^\circ$  in Fig. 8, the underpredicted suction peak of JHh-v2 RSM is not improved by the ADDES approach. However, both the size and the qualitative trend of the measured pressure plateau in the separation area match slightly better.

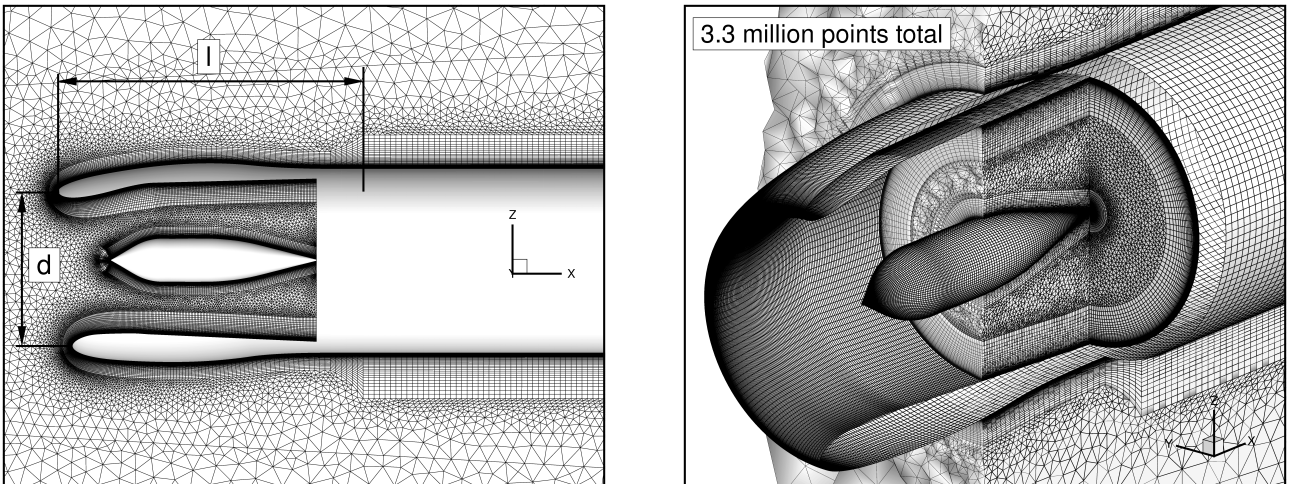


Figure 9: Geometry and numerical mesh for the LARA-nacelle simulations.

## 4 Flow Simulations of the Transonic LARA Nacelle

To assess the RSM-based simulation method for transonic inlet stall, the flow around the laminar-flow nacelle LARA is computed and compared to experiments [5]. Suited measurement data were obtained from off-design studies in realistic flow conditions w.r.t. Reynolds number and mass-flow rates, which could be realized in the pressurized Onera-F1 wind tunnel by mounting the nacelle model on a suction duct. In particular, the experimental setup from the measurement series LOT202 is selected which simulates the critical starting phase of an aircraft with maximum thrust (“rolling take-off”) and exhibits internal inlet separation at high angles of attack. Despite a mostly incompressible onflow with  $Ma = 0.27$ , the flow is strongly accelerated by the suction flow-rate of  $dm/dt \approx 41$  kg/s (for the full  $360^\circ$ -model) and reaches locally supersonic speed near the lower inlet lip. The Reynolds number based on the inlet diameter  $d$  slightly varies throughout the experiment around  $Re_d = 5.3 \cdot 10^6$ .

The measurement data comprise static surface pressure on the nacelle contour as well as total and dynamic pressure in the (virtual) fan plane at various circumferential angles  $\Theta$ . The latter were used to derive distortion coefficients of the fan onflow, which are an important industrial measure to estimate the impact of the disturbed inlet flow on the core engine.

The (U)RANS-based simulations employ the JHh-v2 RSM and the Menter SST model for reference. The considered geometry includes a central body, which was present in the experiment, whereas details of the instrumentation and the suction duct are neglected. Instead, an engine-inflow plane is defined at the end of the central body, and the outer contour downstream of the nacelle length  $l$  is extended by a cylinder, see Fig. 9. The hybrid hexahedral/tetrahedral mesh shown in Fig. 9 contains about 3.3 million grid points in total. Farfield conditions at a sufficient distance from the nacelle confine the flow domain, while TAU’s engine-inflow boundary condition with fixed mass flow is applied at the inflow plane to obtain the given flow rate. The angle of attack is gradually increased from  $\alpha = 20^\circ$  to  $34^\circ$ .

### 4.1 Results

A general overview on the flow topology for the computations with the JHh-v2 RSM is given in Fig. 10 which shows surface streamlines and distributions of the isentropic Mach number

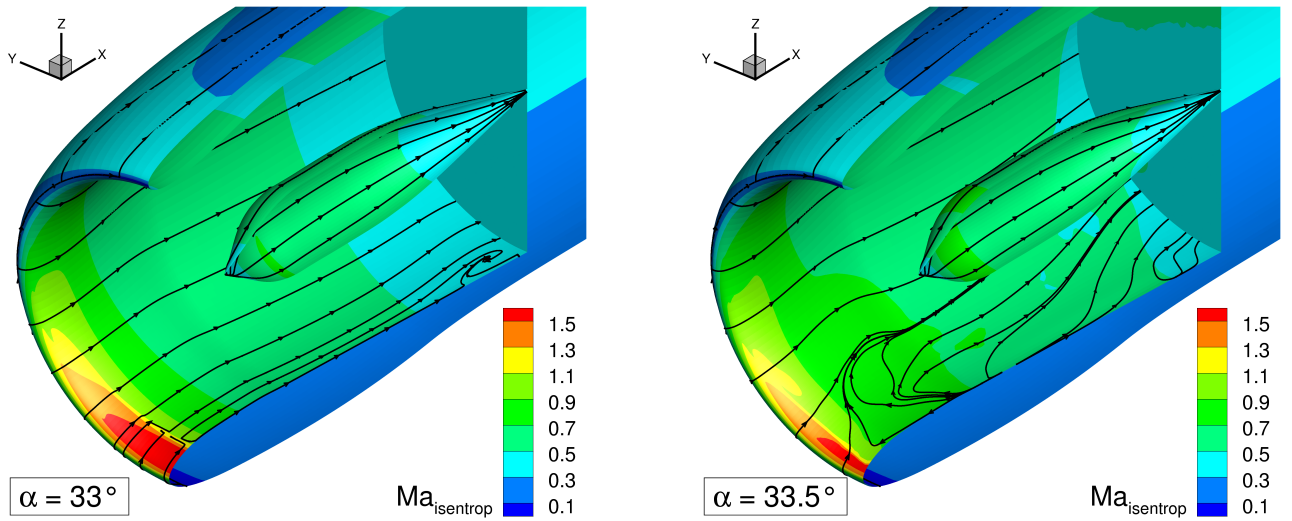


Figure 10: Isentropic Mach-number distribution and surface streamlines on the LARA nacelle computed with the JHh-v2 RSM.

on the inlet contour. Due its careful aerodynamic design the flow in the nacelle remains fully attached even beyond  $\alpha = 30^\circ$ . First local separations are not observed until  $\alpha = 33^\circ$ , where both a shock-induced separation at the leading-edge and a recirculation zone at the engine-inflow are formed right next to the symmetry plane, see Fig. 10, left. Just slightly increasing  $\alpha$  to  $33.5^\circ$ , the flow breaks down to unsteadiness and forms a pronounced separation pattern with a reduced supersonic region, see Fig. 10, right.

Figure 11 compares computed and measured surface-pressure distributions on the nacelle contour in two cut sections of the lower inlet region. Apart from few local deviations, the JHh-v2 RSM computations agree very well with measurements up to  $\alpha = 33^\circ$ . This includes the location and strength of the shock at  $\alpha = 30^\circ$  and above, which is visible in the lower cut section  $\Theta = 180^\circ$  around  $x/l = 0.05$ . The separation onset at  $\alpha = 33.5^\circ$  observed in Fig. 11 results in a sudden drop of the leading-edge pressure minimum and break-down of the shock in the temporal mean. Although the experiments show a similar behaviour, it occurs by about half a degree later ( $\alpha = 33.9^\circ$ ) and appears somewhat less pronounced, when comparing the JHh-v2 RSM results at  $\alpha = 33.5^\circ$  with the measurements at  $\alpha = 33.9^\circ$ .

From an industrial viewpoint, simpler global measures are preferred to characterize the state of the disturbed inlet flow. Exemplarily, the development of the peak Mach numbers at the inlet lip and the so-called distortion coefficients  $DC_{60/120}$  are considered here.

Similar to the pressure distributions, the maxima of the (isentropic) Mach numbers in Fig. 12, left, agree very well with the experiment up to separation onset at  $\alpha = 33.5^\circ$ . The following sudden drop of  $Ma_{peak}$  at  $\Theta = 180^\circ$  by about 40% roughly agrees with the measurements but occurs by about  $\Delta\alpha = 0.5^\circ$  too early, thus confirming the observations above. In all cut sections, the overall qualitative trends are matched well by the JHh-v2 RSM simulations.

The distortion coefficients  $DC_{60}$  and  $DC_{120}$  depend on the maximum difference of the surface-averaged total pressure  $\hat{p}_t$  between the whole fan plane and any possible angular segment of either  $\Delta\Theta = 60^\circ$  or  $120^\circ$ :

$$DC_{60/120} = \frac{\max(\hat{p}_t - \hat{p}_{t,60^\circ/120^\circ})}{\hat{q}} \quad (5)$$

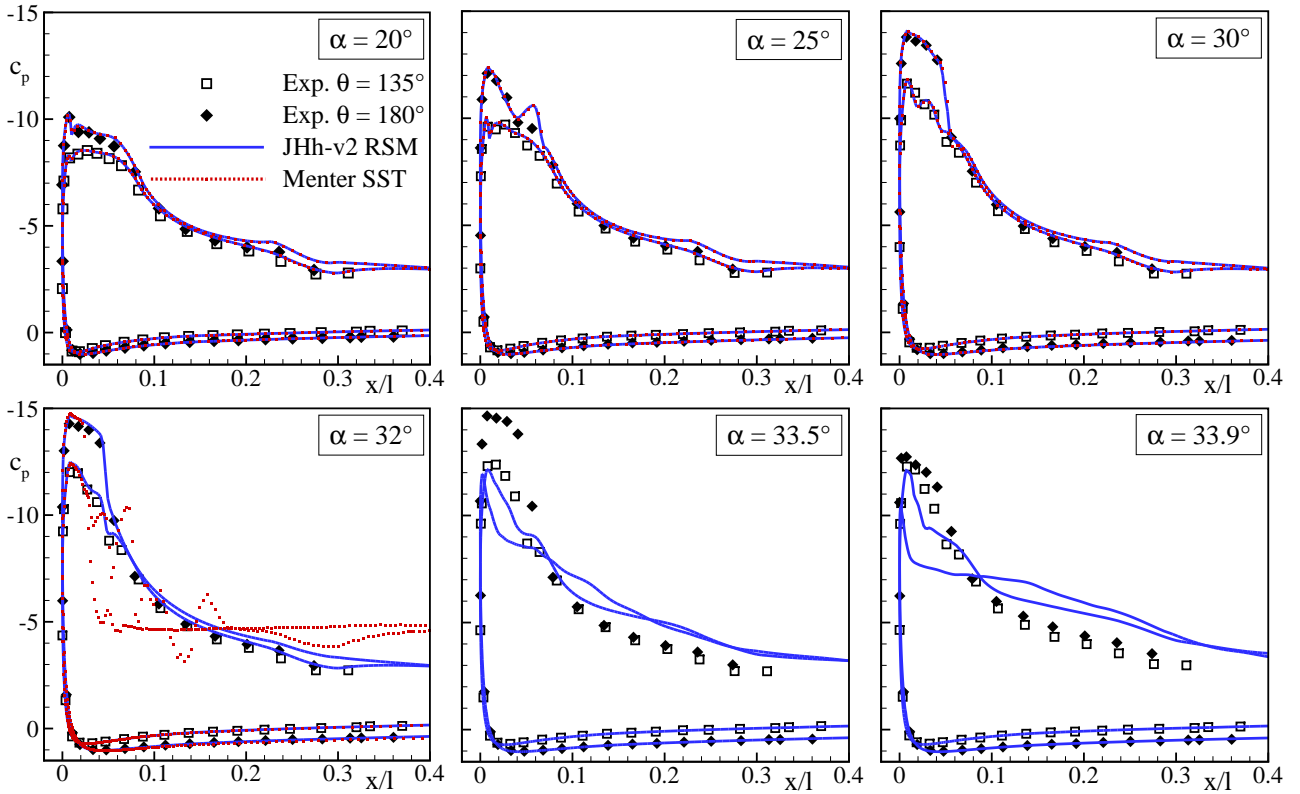


Figure 11: Static surface-pressure distributions on the LARA-nacelle contour at different circumferential angles  $\Theta$ .

The normalization is based on the surface-averaged dynamic pressure  $\hat{q}$  in the fan plane. Thus, both coefficients represent a measure for the total-pressure loss associated with a disturbed (e.g. separated) flow, while their ratio reflects the locality of the distortion. In the present inlet flow, the mostly disturbed fan-plane segments are located in the lower inlet region around  $\Theta = 180^\circ$ . This is due to the strong local pressure rise, see Fig. 11, which leads to a comparably large boundary-layer thickening and eventually separation starting near the symmetry plane, see Fig. 10. Moreover,  $DC_{60}$  generally exceeds  $DC_{120}$ , indicating a local concentration of the distortion in that area.

Apart from a slightly underestimated  $DC_{60}$ -value at  $\alpha = 20^\circ$ , both distortion coefficients computed with the JHh-v2 RSM follow the measurements remarkably well up to  $\alpha = 33^\circ$ , see Fig. 12, right. Then, after rising by more than one order of magnitude just within  $\Delta\alpha = 0.5^\circ$ , they quickly settle on the higher level. The same behaviour is observed in the experiment half a degree later, showing that not only the near-wall flow variables at the inlet lip, but also the off-wall flow field in the fan plane is captured by the JHh-v2 RSM simulations.

Although the overall trends of transonic inlet stall can also be covered with the Menter SST model, its results in Fig. 12, right, shows somewhat larger deviations from the experiments than for the RSM. Besides a slight underestimation of both  $DC_{60}$  and  $DC_{120}$  prior to separation, the subsequent boost in the distortion level is shifted by another  $\Delta\alpha = 0.5^\circ$  compared to the RSM, consequently occurring about  $1^\circ$  earlier than measured. This is also reflected in the pressure distributions for Menter SST in Fig. 11, which shows a large plateau due to separation already at  $\alpha = 33^\circ$ . Note, that this  $c_p$  plot displays an instantaneous result of a time-accurate simulation, illustrating the strong unsteadiness with Menter SST at this angle of attack.

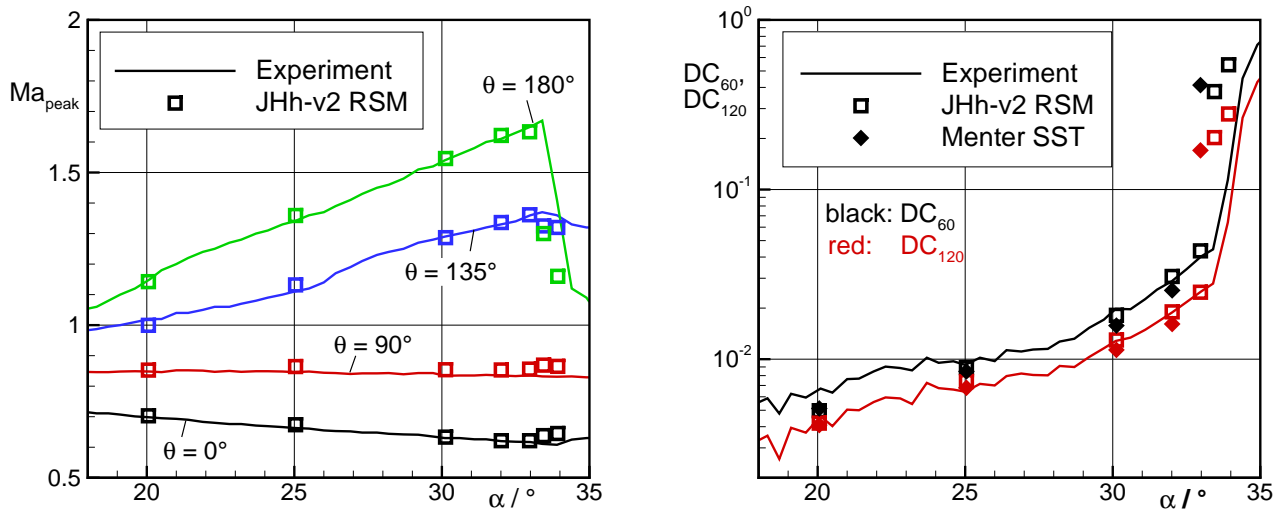


Figure 12: Peak Mach numbers at different circumferential angles  $\Theta$  (left) and distortion coefficients in the fan plane (right) of the LARA nacelle.

## 5 Conclusion

An extended validation of the near-wall Reynolds-stress modelling developed in DFG-FOR1066 was conducted with respect to inlet stall at different speed regimes. In continuation of previous joint research efforts, the validation experiments on a flow-through nacelle were taken as reference case for subsonic stall conditions. The (U)RANS simulations with a recent variant of the JHh-Reynolds-stress turbulence model and linear-stability-based transition modelling was found to predict separation onset close to experimental uncertainty, offering further improvements over an earlier RSM variant and the  $k-\omega$  SST eddy-viscosity model.

However, in the later stages of stall the initially well predicted mean-flow topology begins to deviate from measurements. In comparisons with recent PIV data from the experiment, this behaviour could be traced back to underpredicted Reynolds shear stresses in the separated-flow area. In a pilot application of RSM-based algebraic DDES (JHh-v2 ADDES) to inlet stall, predictions of both the maximum Reynolds-stress level and the flow topology in the inlet could be improved. Besides a successful verification of the algebraic RANS/LES sensors of ADDES for the three-dimensional separation pattern, another remarkable observation concerns the apparent absence of a “grey area” between modelled and resolved turbulence, which may otherwise severely affect the simulation accuracy. Overall, the hybrid RANS/LES modelling is considered a promising extension of the RSM approach, but requires further verification and validation.

In a complementary validation of the RSM-(U)RANS method for transonic inlet stall, the off-design experiments on the powered LARA nacelle were simulated. The mean-flow predictions up to incipient stall are in similar agreement with measurements as for the subsonic case, although the improvement over the conventional  $k-\omega$  SST model is less significant. The onset of massive shock-induced separation is predicted by just about  $\Delta\alpha = 0.5^\circ$  too early, which yields very good reproduction of lip-peak Mach numbers and distortion coefficients  $DC_{60}$  and  $DC_{120}$ .

## Acknowledgments

The members of DFG-FOR 1066 gratefully acknowledge the support of the “Deutsche Forschungsgemeinschaft DFG” (German Research Foundation) which funded this research.

## References

- [1] Colin, Y., Aupoix, B., Boussuge, J.F., Chanez, P.: “Numerical Simulation of the Distortion Generated by Crosswind Inlet Flows”. 18th ISABE Conference, Beijing, China, Sep. 2-7, 2007.
- [2] Cécora, R.-D., Eisfeld, B., Probst, A., Crippa, S., Radespiel, R.: “Differential Reynolds Stress Modeling for Aeronautics”. AIAA-2012-0465, 2012.
- [3] Schulze, S., Kähler, C.J.: “Analysis of the Flow in Stalling Engine Inlet Models with Different Visualization and Measurement Techniques”. Second Symposium “Simulation of Wing and Nacelle Stall”, June 22nd - 23rd, 2010, Braunschweig, Germany, 2010.
- [4] Probst, A., Schulze, S., Radespiel, R., Kähler, C. J.: “Numerical Simulation of Engine-Inlet Stall with Advanced Physical Modelling Compared to Validation Experiments”. To appear in: New Results in Numerical and Experimental Fluid Mechanics VII. Contributions to the 17th STAB/DGLR Symposium Berlin, Germany 2010.
- [5] Lecordix, J. L., Mullender, A., Lecossais, E., Godard, J. L., Hepperle, M.: “Hybrid Laminar Flow Nacelle Design”. ICAS-96-2.3.4, Proceedings of the 20th Congress of the International Council of Aeronautical Sciences, Sorrento, Italy, 8.-13.9.1996.
- [6] Schwamborn, D., Gerhold, T., Heinrich, R.: “The DLR TAU-code: Recent applications in research and industry”. European Conference on Computational Fluid Dynamics ECCOMAS CFD 2006, P. Wesseling, E. Oñate, J. Périaux (Eds), TU Delft, The Netherlands, 2006.
- [7] Jakirlić, S., Hanjalić, K.: “A new approach to modelling near-wall turbulence energy and stress dissipation”. Journal of Fluid Mechanics, 459(1), Cambridge Univ Press., 2002, pp. 139-166.
- [8] Probst, A., Radespiel, R., Rist, U.: “Linear-Stability-Based Transition Modeling for Aerodynamic Flow Simulations with a Near-Wall Reynolds-Stress Model”. AIAA journal, 50(2), American Institute of Aeronautics and Astronautics, 2012, pp. 416-428.
- [9] Knopp, T., Probst, A.: “Numerical Simulation of Engine-Inlet Stall with Advanced Physical Modelling Compared to Validation Experiments”. To appear in: New Results in Numerical and Experimental Fluid Mechanics VII. Contributions to the 17th STAB/DGLR Symposium Berlin, Germany 2010.
- [10] Probst, A., Radespiel, R., Knopp, T.: “Detached-Eddy Simulation of Aerodynamic Flows Using a Reynolds-Stress Background Model and Algebraic RANS / LES Sensors”. AIAA-2011-3206, 2011.
- [11] Schulze, S., Kähler, C.J., Radespiel, R.: “On the Comparison of Stalling Flow-Through Nacelles and Powered Inlets at Take-Off Conditions”. 1st CEAS European Air and Space Conference, Berlin, Germany, Sep. 10-13, 2007.